The Sparkler: Evolved High-redshift Globular Cluster Candidates Captured by JWST

Lamiya Mowla[1,14] , Kartheik G. Iyer[1,14] , Guillaume Desprez[2] , Vicente Estrada-Carpenter[2] , Nicholas S. Martis[2,3] ,
Gaël Noirot[2], Ghassan T. Sarrouh[4] , Victoria Strait[5,6] , Yoshihisa Asada[2,7] , Roberto G. Abraham[1,8] , Gabriel Brammer[9] ,
Marcin Sawicki[2] , Chris J. Willott[3] , Marusa Bradac[10,11] , René Doyon[12] , Adam Muzzin[4] , Camilla Pacifici[13] ,
Swara Ravindranath[13] , and Johannes Zabl[2]

[1] Dunlap Institute for Astronomy and Astrophysics, 50 St. George Street, Toronto, Ontario, M5S 3H4, Canada; lamiya.mowla@utoronto.ca,
kartheik.iyer@dunlap.utoronto.ca,

[2] Department of Astronomy & Physics and Institute for Computational Astrophysics, Saint Mary's University, 923 Robie Street, Halifax, Nova Scotia, B3H 3C3,
Canada

[3] NRC Herzberg, 5071 West Saanich Rd, Victoria, BC, V9E 2E7, Canada

[4] Department of Physics and Astronomy, York University, 4700 Keele St., Toronto, Ontario, MJ3 1P3, Canada

[5] Cosmic Dawn Center (DAWN), Denmark

[6] Niels Bohr Institute, University of Copenhagen, Jagtvej 128, DK-2200 Copenhagen N, Denmark

[7] Department of Astronomy, Kyoto University, Sakyo-ku, Kyoto 606-8502, Japan

[8] David A. Dunlap Department of Astronomy and Astrophysics, University of Toronto, 50 St. George Steet, Toronto, Ontario, M5S 3H4, Canada

[9] Niels Bohr Institute, University of Copenhagen, Blegdamsvej DK-172100 Copenhagen, Denmark

[10] University of Ljubljana, Department of Mathematics and Physics, Jadranska ulica 19, SI-1000 Ljubljana, Slovenia

[11] Department of Physics and Astronomy, University of California Davis, 1 Shields Avenue, Davis, CA 95616, USA

[12] Département de physique, Université de Montréal, Complexe des Sciences, PO Box 6128, Centre-ville STN, Montreal, QC, H3C 3J7, Canada

[13] Space Telescope Science Institute, 3700 San Martin Drive, Baltimore, MD 21218 USA

Abstract

Using data from JWST, we analyse the compact sources ("sparkles") located around a remarkable $z_{spec} = 1.378$ galaxy (the 'Sparkler) that is strongly gravitationally lensed by the $z = 0.39$ galaxy cluster SMACS J0723.3-7327. Several of these compact sources can be cross-identified in multiple images, making it clear that they are associated with the host galaxy. Combining data from JWSTs Near-Infrared Camera (NIRCam) with archival data from the Hubble Space Telescope (HST), we perform 0.4–4.4 μm photometry on these objects, finding several of them to be very red and consistent with the colors of quenched, old stellar systems. Morphological fits confirm that these red sources are spatially unresolved even in the strongly magnified JWST/NIRCam images, while the JWST/NIRISS spectra show [OIII] $\lambda 5007$ emission in the body of the Sparkler but no indication of star formation in the red compact sparkles. The most natural interpretation of these compact red companions to the Sparkler is that they are evolved globular clusters seen at $z = 1.378$. Applying DENSE BASIS spectral energy distribution fitting to the sample, we infer formation redshifts of $z_{form} \sim 7$–11 for these globular cluster candidates, corresponding to ages of ~ 3.9–4.1 Gyr at the epoch of observation and a formation time just ~ 0.5 Gyr after the Big Bang. If confirmed with additional spectroscopy, these red, compact sparkles represent the first evolved globular clusters found at high redshift, which could be among the earliest observed objects to have quenched their star formation in the universe, and may open a new window into understanding globular cluster formation. Data and code to reproduce our results will be made available at http://canucs-jwst.com/sparkler.html.

Unified Astronomy Thesaurus concepts: Globular star clusters (656); James Webb Space Telescope (2291); Galaxy evolution (594); Galaxy clusters (584); Gravitational lensing (670)

Supporting material: machine-readable table

1. Introduction

Despite being the subject of very active research for decades (see, e.g., reviews by Harris & Racine 1979; Freeman & Norris 1981; Brodie & Strader 2006; Forbes et al. 2018), we do not know when, or understand how, globular clusters form. We *do* know that most globular clusters in the Milky Way (MW), and those around nearby galaxies, are very old. The absolute ages of the oldest MW globular clusters, determined by main-sequence fitting and from the ages of the oldest white dwarfs,

are about 12.5 Gyr, corresponding to formation redshifts of $z_{form} \sim 5$. However, the uncertainties in age estimates are relatively large compared to the cosmic age of the universe at high redshifts, and absolute ages corresponding to $z_{form} \sim 3$ (at Cosmic Noon) at the low end, and extending well into the epoch of reionization at the high end ($z_{form} \gg 6$), are plausible (Forbes et al. 2018).

There are two general views on how globular clusters formed. In the first, globular cluster formation is a phenomenon occurring predominantly at very high redshift, with a deep connection to initial galaxy assembly. Ideas along these lines go back to Peebles & Dicke (1968), who noted that the typical mass of a globular cluster is comparable to the Jeans mass shortly after recombination. In this view, globular clusters are a special phenomenon associated with the conditions in the early universe, and their formation channel is different from that driving present-day star formation. The second view associates

---

globular clusters with young stellar populations seen in nearby starbursting and merging galaxies (Schweizer & Seitzer 1998; de Grijs et al. 2001). In this case, globular cluster formation might be a natural product of continuous galaxy evolution in systems with high gas fractions, and globular cluster formation would peak at lower redshifts (Trujillo-Gomez et al. 2021).

We are on the cusp of distinguishing observationally between these two globular cluster formation channels. JWST is capable of observing routinely down to nJy flux levels at wavelengths beyond two microns, and thus of observing globular cluster formation occurring at high redshift (Carlberg 2002; Renzini 2017; Vanzella et al. 2017, 2022). In this paper, we use newly released data from JWST to analyse the nature of the point sources seen around a remarkable multiply imaged galaxy at $z = 1.378$ that we fondly named the "Sparkler". One image of this galaxy is strongly magnified by a factor of $\sim$10–100 (Caminha et al. 2022; Mahler et al. 2022) by the $z = 0.39$ galaxy cluster SMACS J0723.37327 (hereafter SMACS0723). Our goal is to determine whether these point sources are (1) globular clusters, (2) super star clusters in the body of the galaxy, or (3) the product of global star formation in this galaxy being driven by some other mechanism.

Throughout this paper we use AB magnitudes and assume a flat cosmology with $\Omega_m = 0.3$, $\Omega_\Lambda = 0.7$ and $H_0 = 70 \,\mathrm{km\,s^{-1}\,Mpc^{-1}}$.

2. Data

The imaging and wide-field slitless spectroscopy data used for this work are from the JWST Early Release Observations (ERO) program 2736 ("Webb's First Deep Field"; Pontoppidan et al. 2022). The galaxy cluster was observed with all four instruments on JWST. Only Near-Infrared Camera (NIRCam; Rieke et al. 2005) imaging and Near-Infrared Imager and Slitless Spectrograph (NIRISS; Doyon et al. 2012) spectroscopy are used in this paper. NIRCam imaging is available in six broadband filters: F090W, F150W, F200W, F277W, F356W, and F444W. Shallow NIRISS wide-field spectroscopy was obtained in the F115W and F200W filters with the two orthogonal low-resolution grisms to mitigate contamination (Willott et al. 2022). Only the F115W grism data are used in this study, because they were taken with the only filter containing a strong emission line, [OIII] $\lambda5007$. These JWST data are supplemented with Hubble Space Telescope (HST) Advanced Camera for Surveys (ACS) imaging in F435W and F606W from the RELICS program, drizzled to the same pixel grid (Coe et al. 2019).

We reduced all imaging and slitless spectroscopic data together using the grism redshift and line analysis software for space-based spectroscopy package `Grizli`[15] (Brammer & Matharu 2021). We first obtained uncalibrated ramp exposures from the Mikulski Archive for Space Telescopes (MAST[16]), and ran a modified version of the JWST pipeline stage Detector1, which makes detector-level corrections for, e.g., ramp fitting, cosmic ray rejection (including extra "snowball" artifact flagging), dark current, and calculates "rate images". Our modified version of the pipeline also includes a column-average correction for $1/f$-noise. Subsequently, we used the preprocessing routines in `Grizli` to align all of the exposures to the HST images, subtracted the sky background, and drizzled all images to a common pixel grid with a scale of 0.″04

per pixel. For the NIRCam F090W, F150W, and F200W images we created another data product with a 0.″02 pixel scale. The context for the JWST Operational Pipeline (CRDS_CTX) used for reducing the NIRISS (NIRCam) data was `jwst_0932.pmap` (`jwst_0916.pmap`). This is a preflight version of the NIRCam reference files, so the NIRCam fluxes should be treated with caution. One consequence of this is that the NIRCam photometric zero points calculated from our reductions may be incorrect for in-flight performance, so we used `EAZY` (Brammer et al. 2008) to derive zero-point offsets consistent with photometric redshift fitting of the full source catalog. Bright cluster galaxies and the intracluster light were modeled and subtracted out using a custom code (N. Martis et al., in preparation). To enable measurement of accurate colors our analysis was done after convolution by a kernel to match the point-spread function (PSF) of F444W.

Figure 1 shows images of the Sparkler. The coordinates for the three images of the background galaxy are presented in the caption accompanying the figure. The Sparkler was first identified as multiply imaged in HST imaging combined with ESO MUSE integral-field spectroscopy that shows all three images having [OII] $\lambda3727$ emission (Golubchik et al. 2022). We adopt the spectroscopic redshift of $z = 1.378 \pm 0.001$ obtained from the MUSE [OII] $\lambda3727$ line (Caminha et al. 2022; Golubchik et al. 2022; Mahler et al. 2022). The magnifications of the three images (labeled as 1, 2, and 3 in Figure 1) in the lensing model of Mahler et al. (2022; their IDs 2.1, 2.2, and 2.3) are 3.6 ± 0.1, 14.9 ± 0.8, and 3.0 ± 0.1, respectively. In the lensing model of Caminha et al. (2022; their IDs 3a, 3b, and 3c) the magnifications are significantly higher: $9.2^{+1.3}_{-1.2}$, 103^{+153}_{-47}, and $6.1^{+0.7}_{-0.7}$, respectively. Based on the measured flux ratios between the three images we consider the Caminha et al. (2022) model to fit the properties of this galaxy better. As shown in Figure 1, there may be critical curves and/or high-magnification contours crossing image 2 (a magnification of 5–10 in the Mahler et al. 2022 model and a magnification of 30–100+ in the Caminha et al. 2022 model), suggesting strong differential magnification in the image. Figure 2 shows a multiband montage of image 2 of the Sparkler, using data from HST/ACS, HST/WFC3, and JWST/NIRCam short- and long-wavelength cameras at observed wavelengths spanning 0.4–4.4 μm. Circles in the lower-left of each panel show the FWHM of the PSF which range from 0.″034 for NIRCam/F150W to 0.″145 for NIRCam/F444W.[17] The exquisite resolution of JWST/NIRCam's short wavelength data best reveals the compact sources surrounding the galaxy, which were not resolved by HST in earlier observations, even at similar wavelengths.

3. Methods

In this letter we focus our attention on twelve compact candidates in and around image 2 of the Sparkler, at least seven of which are confirmed to be unique from image 1. In this preliminary exploration, we selected candidates by eye, focusing mainly on compact objects ("sparkles") in uncontaminated regions of the image. A few compact sources in the galaxy itself were also added to our sample to allow us to compare objects in the body of the Sparkler to objects in the periphery of the galaxy. Objects were selected using the very
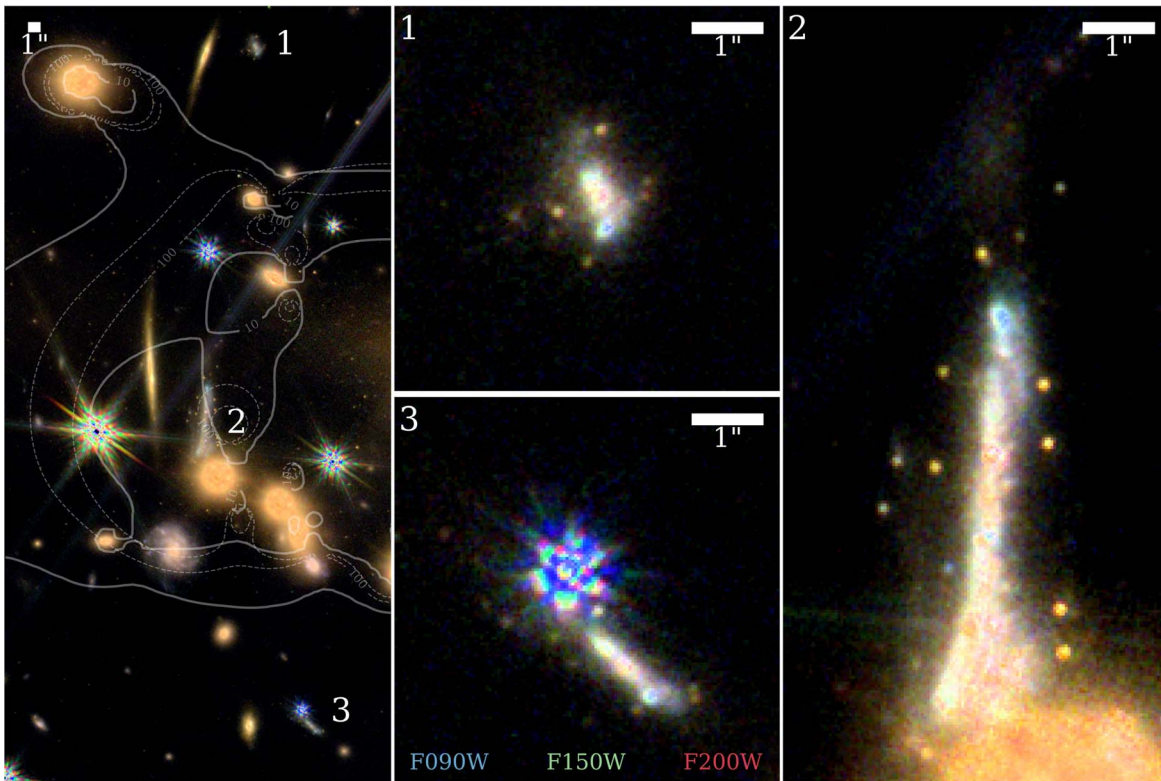

Figure 1. Color images of the Sparkler and its environs made by combining F090W, F150W, and F200W images at native spatial resolution. The left panel shows the region around the three images of the Sparkler, with lines of lensing magnification from the Mahler et al. (2022; solid curves) and Caminha et al. (2022; dashed curves) models overlaid. Note that regions of very strong magnification ($\mu \sim 10\text{--}100$) cross image 2 of the Sparkler. The remaining three panels zoom in on the three images of this galaxy. Images are centered on the following positions. Image 1: R.A. = 110.83846, decl. = −73.45102; image 2: R.A. = 110.84051, decl. = −73.45487; and image 3: R.A. = 110.83614, decl. = −73.45879. Note the compact sources, many of them red, surrounding the body of the galaxy; these are most prominent in image 2, but are also discernible in images 1 and 3.

deep $0\rlap{.}''02$ pixel scale F150W image, and were chosen to be broadly representative of the compact sources in this system. As described below, 2D modeling confirms that the objects chosen are unresolved. We emphasize that the objects analysed in this letter are not a complete sample, and as the main galaxy is close to (though likely outside) a fold caustic, it is also possible that some of the sparkles are multiple images of each other. Construction of a complete sample and their stellar mass surface densities will require detailed background subtraction and foreground galaxy lens modeling, which is deferred to a future paper.

3.1. Aperture Photometry

Photometry is challenging in crowded fields, and in the case of the Sparkler the challenges are compounded by contamination from the host galaxy and from other nearby sources. This contamination can significantly alter the shape of the SED of the individual compact sources. In a future paper we will present a full catalog of compact sources around the Sparkler that attempts to account for these effects by subtracting contamination models and using PSF photometry. For simplicity and robustness, in the present paper we used aperture photometry, as this technique is relatively insensitive to variations in the local background. Photometry was done using images that (1) are on $0\rlap{.}''04$ pixel scale, (2) have a bright cluster galaxy and intracluster light-subtracted, and (3) are F444W PSF-convolved F435W, F606W, F090W, F150W, F200W, F277W, F356W, and F444W images.

Using `photutils` (Bradley et al. 2021), circular apertures with radii of $0\rlap{.}''12$, $0\rlap{.}''16$, and $0\rlap{.}''20$ were defined using the centroided positions of the twelve sparkles in the F150W image. An annulus starting at the edge of the aperture and with a width of $0\rlap{.}''08$ was used to estimate the median local background, which was subtracted from the aperture flux. Aperture correction was applied by multiplying by the F444W PSF growth curve. To determine contamination corrections, we injected simulated point sources of various fluxes around the galaxy to determine how well our procedure recovered the intrinsic total flux of the compact sources. We found that the precision of the photometry varied widely across the different filters, environments, and intrinsic brightnesses of the sources, but that these variations could be quantified by simulations. For every sparkle, we identified a location proximate to it in which we injected simulated point sources to model the measurement accuracy. For a sparkle at a given wavelength, we injected 20 point sources of total flux varying between 0.1 and 10 times the measured flux of the source and measured their fluxes using the same techniques used to analyse the original sources. We then fit the intrinsic flux as a function of the measured flux with a second-order polynomial, which we used to determine local aperture corrections. This process was repeated across 20 different locations around the galaxy to estimate the uncertainty in the flux measurement. We selected the $0\rlap{.}''20$ aperture for our final photometry as the corrected flux recovered $>99\%$ of the intrinsic flux across all environments. The procedure was performed for all twelve sparkles in all eight filters to construct the final SED of the sources. For sources that are undetected,
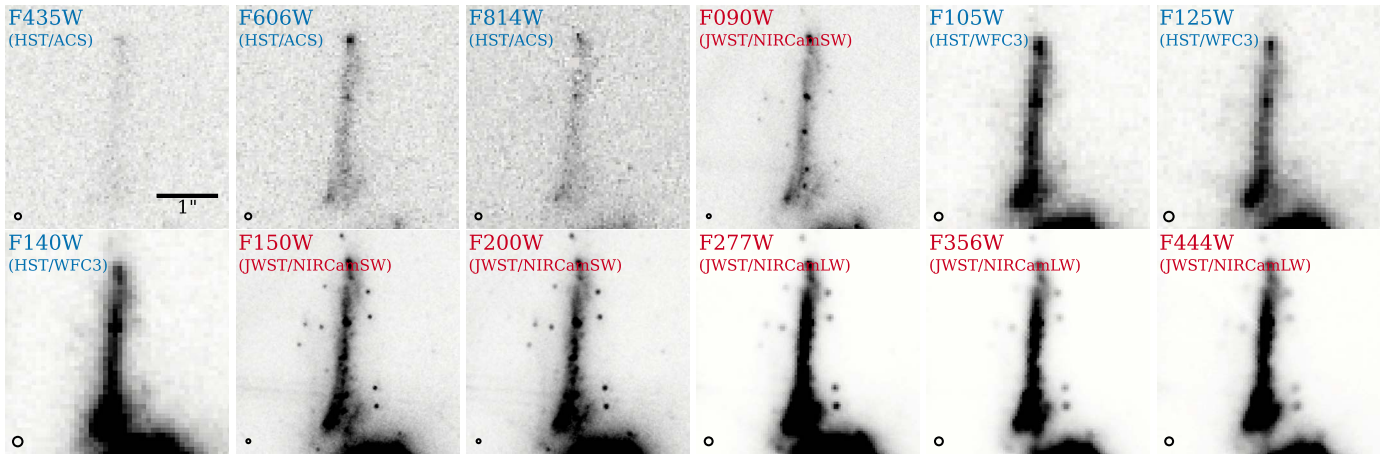
Figure 2. Image 2 of the Sparkler from HST/ACS, HST/WFC3, and JWST/NIRCam short wavelength (SW) and long wavelength (LW) at observed wavelengths from 0.4 to 4.4 μm. Circles in the lower-left of each panel show the FWHM of the PSF which ranges from 0.″034 to NIRCam/F150W to 0.″145 for NIRCam/F444W. Note the exquisite resolution of JWST/NIRCamSW, which reveals the compact sources surrounding the galaxy, which were not resolved by HST in earlier observations at similar wavelengths.

we assigned an upper limit of three times the noise of the image.

3.2. SED Fitting and Estimating the Physical Properties

Spectral energy distributions (SEDs) derived from our aperture photometry were analysed using the DENSE BASIS method[18] (Iyer & Gawiser 2017; Iyer et al. 2019) to determine nonparametric star formation histories (SFHs), masses, ages, metallicities, and dust extinction values for our compact sources. The DENSE BASIS fits were run with a single t_{50} parameter, following the prescription of Iyer et al. (2019), with the full methodology and validation tests presented by Iyer et al. (2018, 2019) and Olsen et al. (2021). The primary advantages of using nonparametric SFHs is that they allow us to account for multiple stellar populations, robustly derive SFH-related quantities including masses, star formation rates (SFRs), and ages, and allow us to set explicit priors in SFH space to prevent outshining due to younger stellar populations that could otherwise bias the estimates of these properties (Iyer & Gawiser 2017; Leja et al. 2019; Lower et al. 2020).

However, DENSE BASIS, by design, implements correlated SFRs over time, to encode the effects of physical processes in galaxies that regulate star formation better, and to recover complex SFHs containing multiple stellar populations better (Iyer et al. 2019). The formalism smooths out SFHs that are instantaneous pulses, and has an age resolution of about 0.5 Gyr. We therefore also undertook SED fits based on simple luminosity evolution of simple stellar populations (SSPs). As will be seen below, in several cases the DENSE BASIS fit results return SFHs that are as close to instantaneous pulses as the method allows. In such cases, the SSP fits may give comparably good results with fewer assumptions. SSP fits also have the benefit of returning unambiguously defined ages. Since the DENSE BASIS fits provide a full SFH posterior, we will define the "age" from these fits to be the time at which the SFR peaks (t_{peak}). Using validation tests fitting synthetic SSP sources injected into the field and mock photometry with similar noise properties to the observed sources, we find that this can robustly recover the age of the corresponding SSP within uncertainties, finding a bias and scatter of

$(\mu, \sigma)_{t_{50}} \equiv (0.15, 1.00)$ Gyr, $(\mu, \sigma)_{t_{peak}} \equiv (0.13, 0.86)$ Gyr, and $(\mu, \sigma)_{age_{SSP}} \equiv (-0.20, 0.86)$ Gyr for the three metrics tested.

3.3. Grism Extraction and Fitting

Before extracting the individual NIRISS spectra, we constructed a contamination model of the entire field using `Grizli`. We modeled the sources at both grism orientations. This model was built using a segmentation map and photometric catalog created with SEP (Barbary 2016; Bertin & Arnouts 1996). We initially assumed a flat spectrum, normalized by the flux in the photometric catalog, in our models. Successive higher-order polynomials were then fit to each source, iteratively, until the residuals in the global contamination model were negligible.

After the spectral modeling of the full field for contamination removal, we then extracted the 2D grism cutouts of the three images of the Sparkler and fitted their spectra using the `Grizli` redshift-fitting routine with a set of FSPS and emission-line templates. `Grizli` forward modeled the 1D spectral template set to the 2D grism frames based on the source morphologies in the direct imaging. `Grizli` identified a redshift solution for the Sparkler based on the identification of [O III] $\lambda5007$ at 1.2 μm in the F115W grism data. This is consistent with the identification of the complementary [O II] $\lambda3727$ line previously reported in the MUSE data, and securely confirms the spectroscopic redshift of the source as $z = 1.38$. As a product of the fitting, emission-line maps of the [O III] $\lambda5007$ line were created for the three images of the Sparkler.

4. Results

The fluxes and associated uncertainties for the twelve compact sources (sparkles) in and around the Sparkler are presented in Table 1, and their positions are identified in image 2 of the Sparkler in the middle row of panel (a) in Figure 3. Panel (b) of this figure shows point source fits (using GALFIT; Peng et al. 2010) to several sparkles in our sample. Residuals from the fits are negligible, confirming the original visual impression that these compact sources are unresolved. Panel (c) in Figure 3 shows the colors of the individual sparkles in the rest-frame *urJ* color–color space (measured directly from

---

Table 1
Observed Photometric Properties and Derived Physical Parameters for the Compact Point Sources Estimated from DENSE BASIS and the SSP Fitter

ID	1	2	3	4	5	6	7	8	9	10	11	12
Class[a]	GC	GC	C	GC	E	E	B	GC	C	GC	B	B
F_ν [nJy; F435W]	⋯	⋯	⋯	⋯	⋯	⋯	13.98	33.51	⋯	⋯	38.17	155.42
δF_ν [nJy; F435W]	⋯	⋯	⋯	⋯	⋯	⋯	±4.57	±4.72	⋯	⋯	±4.57	±4.63
F_ν [nJy; F606W]	⋯	⋯	⋯	⋯	20.28	20.98	21.20	⋯	⋯	⋯	102.37	231.08
δF_ν [nJy; F606W]	⋯	⋯	⋯	⋯	±3.24	±3.28	±3.16	⋯	⋯	⋯	±3.15	±3.08
F_ν [nJy; F814W]	⋯	⋯	⋯	⋯	52.41	⋯	46.52	⋯	67.55	⋯	126.44	258.67
δF_ν [nJy; F814W]	⋯	⋯	⋯	⋯	±4.49	⋯	±4.54	⋯	±4.58	⋯	±4.62	±4.54
F_ν [nJy; F090W]	2.40	3.00	19.05	⋯	25.70	17.66	72.54	17.40	6.40	7.45	178.21	249.38
δF_ν [nJy; F090W]	±2.27	±2.26	±2.34	⋯	±2.41	±2.42	±1.78	±2.30	±2.35	±2.34	±1.77	±1.87
F_ν [nJy; F150W]	20.12	17.11	22.25	35.21	48.47	34.82	69.74	77.23	19.80	52.99	285.08	334.33
δF_ν [nJy; F150W]	±5.32	±5.33	±5.28	±5.28	±5.28	±5.28	±5.35	±5.29	±5.25	±5.29	±5.35	±5.32
F_ν [nJy; F200W]	41.05	72.04	41.53	35.97	44.43	32.12	82.67	91.62	22.36	60.53	328.86	271.68
δF_ν [nJy; F200W]	±5.03	±5.04	±5.09	±5.12	±5.09	±5.14	±5.07	±5.08	±5.11	±5.08	±5.07	±5.04
F_ν [nJy; F277W]	51.28	67.68	73.76	75.72	60.01	33.99	60.36	104.96	21.52	82.81	455.34	351.27
δF_ν [nJy; F277W]	±7.21	±7.19	±7.24	±7.23	±7.24	±7.34	±7.10	±7.25	±7.33	±7.23	±7.04	±7.06
F_ν [nJy; F356W]	46.60	95.96	55.93	58.01	57.21	27.74	98.49	111.25	10.54	88.50	502.32	345.09
δF_ν [nJy; F356W]	±7.20	±7.21	±7.17	±7.21	±7.21	±7.16	±7.03	±7.20	±7.14	±7.21	±6.44	±6.98
F_ν [nJy; F444W]	25.70	61.42	62.45	68.21	53.26	26.67	43.28	75.12	12.08	74.95	452.73	311.93
δF_ν [nJy; F444W]	±6.23	±6.16	±6.21	±6.22	±6.62	±6.13	±6.09	±6.21	±6.17	±6.22	±6.10	±6.07
$\log M_{*,50}$[b] $[M_\odot]$	8.26	8.57	8.42	8.57	8.34	8.15	8.20	8.68	7.96	8.58	9.09	8.41
$\log M_{*,16}$[b] $[M_\odot]$	8.15	8.48	8.32	8.48	8.24	8.01	7.72	8.60	7.82	8.49	9.01	8.33
$\log M_{*,84}$[b] $[M_\odot]$	8.38	8.67	8.52	8.68	8.45	8.27	8.34	8.77	8.10	8.67	9.14	8.49
$\log sSFR_{*,50}$ $[yr^{-1}]$	−12.05	−12.25	−12.05	−12.15	−11.55	−11.05	−8.95	−12.45	−11.75	−12.25	−9.25	−8.35
$\log sSFR_{*,16}$ $[yr^{-1}]$	−13.25	−13.35	−13.25	−13.35	−13.15	−12.95	−9.75	−13.35	−13.15	−13.35	−9.35	−8.45
$\log sSFR_{*,84}$ $[yr^{-1}]$	−10.85	−11.05	−10.85	−10.95	−10.05	−9.55	−8.05	−11.35	−10.35	−11.15	−9.05	−8.25
$t_{peak, 50}$ [Gyr]	4.10	4.01	0.68	3.87	0.32	0.87	0.27	4.06	4.01	4.10	0.05	0.00
$t_{peak, 16}$ [Gyr]	2.60	2.51	0.68	2.27	0.32	0.07	0.27	2.46	3.01	2.60	0.05	0.00
$t_{peak, 84}$ [Gyr]	4.51	4.51	1.98	4.37	2.02	2.67	0.52	4.51	4.51	4.51	3.60	0.00
$A_{V,50}$ [mag]	0.30	0.48	0.28	1.28	0.15	0.16	0.18	0.23	0.22	0.34	0.27	0.03
$A_{V,16}$ [mag]	0.08	0.16	0.07	0.78	0.04	0.04	0.03	0.06	0.06	0.10	0.20	0.01
$A_{V,84}$ [mag]	0.68	0.91	0.62	1.82	0.39	0.47	0.49	0.49	0.55	0.71	0.35	0.05
$\log Z_{50}/Z_\odot$	−0.51	−0.33	−0.47	−0.11	−1.04	−1.02	−0.82	−0.72	−0.72	−0.36	0.21	0.11
$\log Z_{16}/Z_\odot$	−1.09	−0.88	−1.05	−0.67	−1.37	−1.37	−1.43	−1.13	−1.25	−0.89	0.14	0.09
$\log Z_{84}/Z_\odot$	−0.02	0.05	0.01	0.16	−0.45	−0.41	−0.54	−0.24	−0.12	0.03	0.24	0.15
$\log M_{*,SSP}$ $[M_\odot]$	8.66	8.87	8.41	8.98	8.49	8.23	8.45	9.06	8.34	8.97	8.60	8.32
age_{SSP} [Gyr]	4.37	3.16	1.26	4.50	0.56	0.71	0.39	4.47	4.47	4.50	0.04	0.03
$\log Z/Z_{\odot,SSP}$	−0.50	−0.26	−0.55	0.00	−1.47	−1.50	−1.50	−1.00	−1.50	−0.50	0.00	0.00
$A_{V,SSP}$ [mag]	0.11	0.43	0.23	1.00	0.60	0.22	0.00	0.12	0.00	0.18	0.71	0.06
χ^2_{DB}/χ^2_{SSP}	1.01	1.03	1.27	1.00	1.05	0.95	0.72	0.92	0.94	0.93	0.51	2.02

Notes. Reported uncertainties represent the 16th–84th percentiles of the posterior distribution for each quantity.
[a] Categories for the individual objects: GC: globular cluster candidates; C: possibly contaminated by galactic light (or by a nearby diffraction spike for id 9); E: extended sources from visual inspection; B: in the bulk of the galaxy or actively star-forming, for e.g., the OIII regions in Figure 4.
[b] The stellar masses account for stellar mass loss but are not corrected for magnification factors, which are ∼10–100 and can vary across the image.

(This table is available in its entirety in machine-readable form.)

F090W, F200W, and the average of the F277W and F356W fluxes), overplotted on the distribution of $z \sim 1.4$ galaxies from the COSMOS2020 catalog (Weaver et al. 2022). The body of the Sparkler galaxy (blue point) is in the star-forming blue cloud, as are 7 of 12 of our sparkles (orange points). However, five of the sparkles have red colors ($u^* - r > 1.5$) consistent with those of quiescent systems (so-called red clouds). These five red, unresolved objects will constitute our sample of globular cluster candidates throughout this paper, and are color-coded in pink in all figures in this paper.

The SEDs and derived SFHs inferred from our modeling are shown in Figure 4. The physical properties corresponding to the models shown in this figure are also given in Table 1. The table contains the effective ages of the globular cluster candidates from both the DENSE BASIS and SSP fitting methods, which generally agree within the uncertainties. Of the objects under consideration, six (IDs 1, 2, 4, 8, 9, and 10) are consistent with SFHs that peaked at early formation times. Note that we do not include object 9 in our list of globular cluster candidates because of its low signal-to-noise ratio (S/N), coupled with possible contamination from the nearby diffraction spike and extended tail visible in Figure 1. Objects 11 and 12, which are in the bulk of the galaxy, show recent star formation, consistent with the [OIII] $\lambda5007$ emission in Figure 3. While these could be younger star clusters that might evolve into globular clusters, they happen to be completely overlapping with the bulk of the galaxy, and disentangling the light of the compact source from that of the
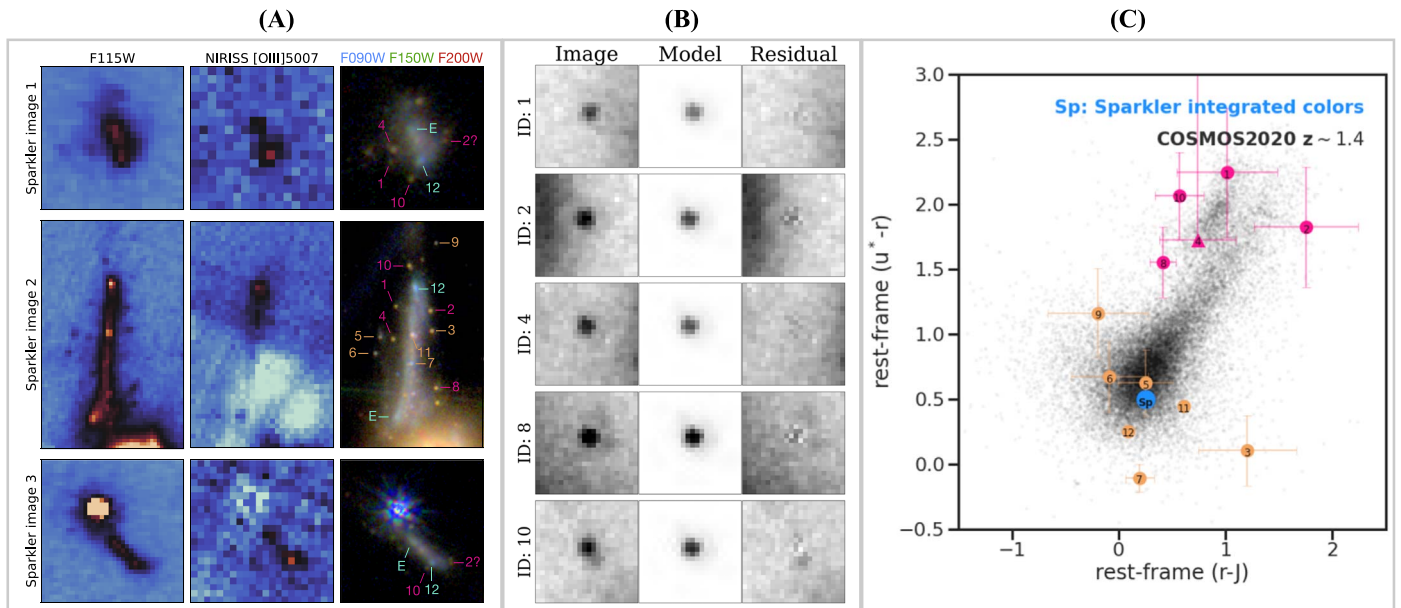
(A)

(B)

(C)

Figure 3. (a) The globular cluster candidates associated with the main galaxy. Shown are the F115W images (left column), [OIII] λ5007 emission-line maps derived from the NIRISS grism data in the F115W band (middle column), and NIRCam color composite images (right column). Sparkle IDs are shown for image 2, with tentative counterparts identified in images 1 and 3. The lower part of the [OIII] λ5007 map of image 2 suffers from significant contamination. [OIII] λ5007 emission is a classic signature of ongoing star formation; here, it is present in the star-forming regions of the host galaxy, but its absence at the locations of the globular cluster candidates supports the hypothesis that at the epoch of observation these are quiescent systems. (b) The globular cluster candidates are unresolved. Fits to the globular cluster candidates with point sources on the 0″02 F150W images using GALFIT (Peng et al. 2010) show that the residuals are consistent with noise. (c) The globular cluster candidates have colors of quenched stellar systems. The *urJ* colors (measured directly from F090W, F200W, and the average of the F277W and F356W fluxes) compared with z ∼ 1.4 galaxies in the "Classic" COSMOS2020 catalog (Weaver et al. 2022). The integrated colors of the Sparkler galaxy (blue circle labeled as "Sp") are in the star-forming blue cloud, as are our other point sources (orange), but the globular cluster candidates (pink) have *u*-*r* > 1.5 and are consistent with the colors of quenched systems.

host is extremely difficult. As a result, the star formation measured from the photometry is likely a combination of light from both sources, which makes it difficult to speculate on their nature as younger star clusters. With a larger data set of similar galaxies from JWST observations such as presented by Laporte et al. (2022), it might be possible to observe the formation and evolution of globular clusters as it happens, and at higher redshifts than previously possible.

Panel (a) of Figure 3 shows emission-line maps at the redshifted wavelength of [OIII] λ5007 for all three images of the Sparkler. Individual columns show the direct, F115W image (the broadband filter within which the redshifted [OIII] λ5007 emission lies), and a NIRCam F090W, F150W, and F200W color composite for each Sparkler image. There is clear evidence of [OIII] λ5007 emission in all three images, which we interpret as related to star formation activity in the Sparkler. Note that the line emission is spatially with the two blue regions in the color composite, consistent with this interpretation. Most importantly, there is no evidence of line emission at the locations of those sparkles that we have previously identified as globular cluster candidates (IDs 1, 2, 4, 8, and 10), and this adds confidence to our conclusion that these objects consist of old stellar populations and are devoid of ongoing star formation.

Much can be learned from inter-comparing the images shown in panel (a) of Figure 3, and in particular, from comparing the properties of sparkles we identified in image 2 with their counterparts in images 1 and 3. We leave such analysis, as well as the construction of a full lens model of the system, to future papers; for now, we simply highlight a few tentatively matched features in the third column of this panel,

focusing on the globular cluster candidates (pink labels) and the two most prominent star-forming regions (cyan labels).

We close this section with some preliminary discussion of the mass of the Sparkler. Fits to the integrated photometry of images 1 and 3 using DENSE BASIS recover log stellar masses of $9.67^{+0.08}_{-0.09} M_\odot$ and $9.51^{+0.08}_{-0.08} M_\odot$, respectively for the host galaxy (uncorrected for magnification), and SFHs that show a recent rise over the last ∼Gyr. We do not fit image 2 due to the strong differential magnification. Assuming a magnification of ∼5 for image 1 (the average magnification from the Caminha et al. (2022) and Mahler et al. (2022) models), the stellar mass of Sparkler would be around $10^9 M_\odot$, which is similar to that of the Large Magellanic Cloud (Erkal et al. 2019), which has ∼40 globular clusters (Bennet et al. 2022).

5. Discussion

We are at the earliest stages of understanding how best to calibrate the in-flight data from JWST, so the SED modeling is best approached with a degree of caution. For this reason, we emphasize that our most important conclusions spring from observations that are independent of detailed SED modeling. First, many of the compact sources in and around the Sparkler are unresolved (panel (b) of Figure 3) and several can be cross-identified in multiple images (Figure 1 and panel (a) in Figure 3), so they are clearly associated with the host galaxy, placing them at z = 1.378. The colors of these systems are consistent with the expected positions of quiescent sources at z = 1.378 on a rest-frame *urJ* diagram (panel (c) of Figure 3). Independent of any modeling, these facts suggest an identification of the red sparkles with evolved globular clusters.
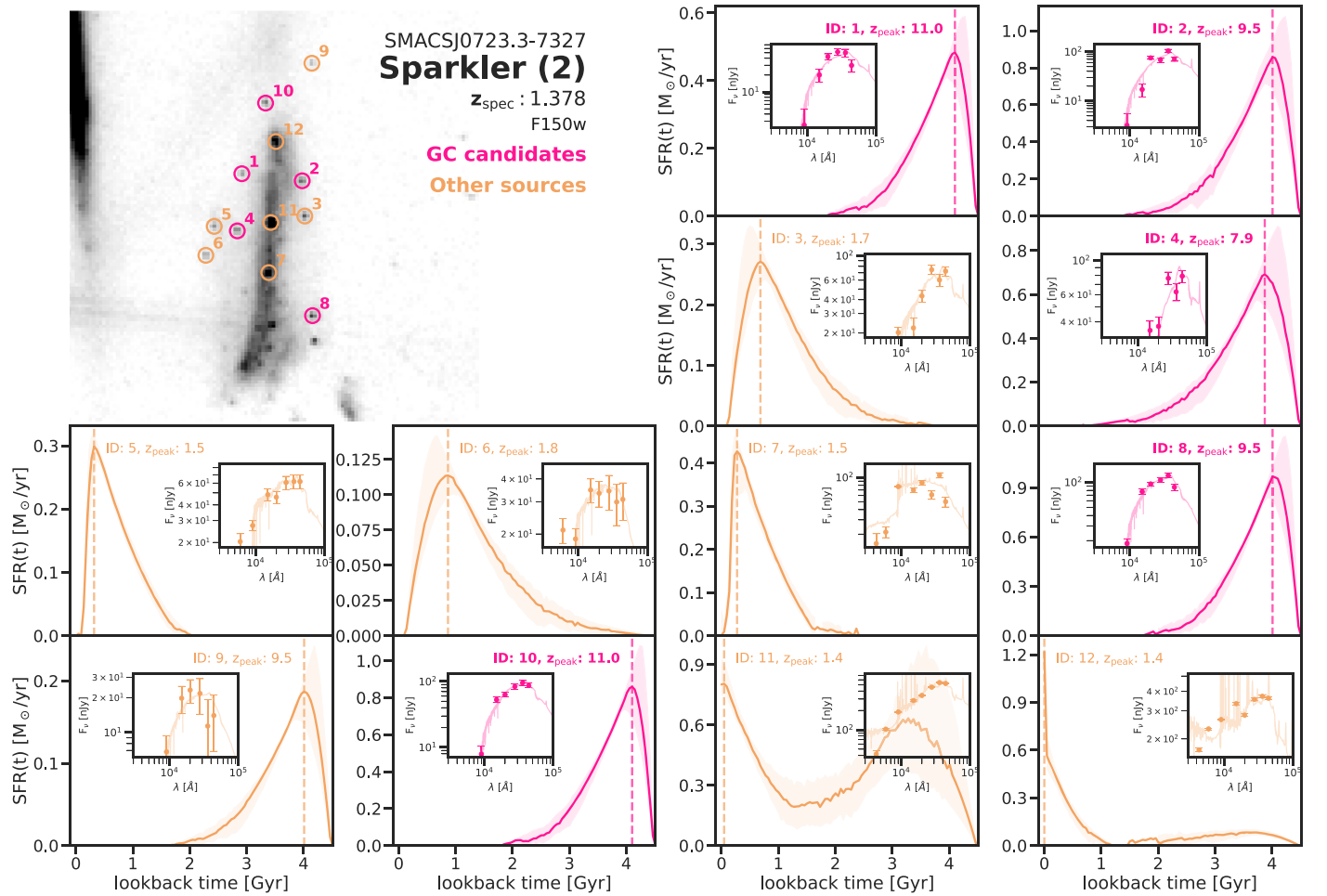
Figure 4. Nonparametric SFHs derived from fitting the photometric SEDs of the individual sparkles. Pink points and curves show the locations and colors (top left), SFHs (marked panels), and SED fits (inset panels) of the individual globular cluster candidates, while orange is used to show the fits and SFHs for objects that are extended sources, heavily contaminated by light from the galaxy, nearby objects or ICL, or in the body of the main galaxy. Even though object 9 is consistent with an early SFH, we exclude it as a globular cluster candidate due to its low S/N and possible contamination by a nearby diffraction spike. The SEDs are shown in F_ν units, with the spectra corresponding to the best-fit model from DENSE BASIS. The SFR values are not corrected for lensing magnification, which could make them $\sim$10–100 times smaller. z_{peak} corresponds to the redshift at which the posterior SFH peaks in SFR. Overall, the globular cluster candidates show SFHs consistent with very early epochs of star formation ranging over $7 < z < 11$.

Going further than this requires modeling. At face value, the reddest compact clumps (5 of the 12 in Table 1 and Figure 4) surrounding the Sparkler show SFHs consistent with SSPs formed at very high redshifts ($z \gtrsim 9$). Another two objects, mainly in the bulk of the galaxy, show SFHs consistent with younger ($\sim$0.03–0.3 Gyr) stellar populations. A primary determinant of these compact sources being globular clusters rather than satellite dwarf galaxies are the sizes and stellar mass surface densities. However, given the limits of JWST's resolution and the uncertainties in lens modeling, a full analysis of these quantities is beyond the scope of this work. Assuming that the sparkles are smaller than the FWHM of the NIRCam/F150W PSF (FWHM $\sim 0''\!.05$) we calculate an upper limit on the sizes of these objects to be $\sim$2–22 pc for the $\mu = 10$ and $\mu = 100$ cases respectively. This results in stellar mass surface densities of $\Sigma \sim 0.7-7 \times 10^4 M_\odot/\mathrm{pc}^2$ or higher, consistent with being globular clusters (Carballo-Bello et al. 2012) rather than dwarf satellites (Herrmann et al. 2016).

The quiescent nature of the reddest point sources in and around the Sparkler effectively rules out the possibility that they are active star formation complexes of the kind seen in many $1 < z < 3$ galaxies, such as those associated with

dynamical instabilities in gas-rich turbulent disks (Förster Schreiber et al. 2006; Genzel et al. 2006). A number of studies examining clumps in high-redshift systems with strong gravitational lensing have been able to explore the clump size distribution at physical spatial resolutions below 100 pc (e.g., Livermore et al. 2012; Wuyts et al. 2014; Livermore et al. 2015; Johnson et al. 2017; Welch et al. 2022a). These report a broad range of sizes (50 pc–1 kpc), but because of the high magnification of the Sparkler, most such clumps would be expected to be resolved by the JWST data we study. As already noted, the pioneering work by Johnson et al. (2017) and Vanzella et al. (2017) suggests that HST observations of strongly lensed active star formation complexes in galaxies at $2 < z < 6$ may already have captured the earliest phases of globular cluster formation. More recent work on lensed $z \sim 6$ galaxies has revealed even smaller complexes, e.g., in the Sunrise Arc (Welch et al. 2022b). This work is exciting, but the association of young massive clusters at high redshift with proto-globular clusters remains indirect, and the future evolution of these star formation complexes is unclear.

The most interesting interpretation of the clumps in and around the Sparkler is that the bulk of them are evolved

(maximally old, given the 4.6 Gyr age of universe at the epoch of observation) globular clusters. This is also consistent with Sameie et al. (2022), who find that globular cluster formation in lower-mass galaxies occurs at redshifts of $\sim 5–10$. If this interpretation is correct, JWST observations of quiescent, evolved globular clusters around $z \sim 1.5$ galaxies can be used to explore the formation history of globular clusters in a manner that is complementary to searching directly for the earliest stages of globular cluster formation (e.g., by examining young massive star formation complexes at $z \sim 6$ and higher; Boylan-Kolchin 2017, 2018). Young star formation complexes may, or may not, evolve eventually into globular clusters, but there can be little doubt about the identity of an isolated and quiescent compact system if its mass is around $10^6 \, M_\odot$ and its scale length is a few parsecs. JWST observations of evolved globular clusters at $z \sim 1.5$ are also complementary to exploring the ages of local globular clusters, as models fit to local globular clusters cannot distinguish between old and very old systems. For example, distinguishing between an ~ 11.5 Gyr old stellar population that formed at $z = 3$ and a 13.2 Gyr old stellar population that formed at $z = 9$ is not possible with current models and data, because they are degenerate with respect to a number of physical parameters (Ocvirk et al. 2006; Conroy et al. 2009, 2010). JWST observations of evolved globular clusters, seen when the universe was about one third of its present age, provide an opportunity for progress by "meeting in the middle", because population synthesis models of integrated starlight from SSPs can distinguish rather easily between the ages of young-intermediate stellar populations. This is because intermediate-mass stars with very distinctive photospheric properties are present at these ages. At $z = 1.378$, the lookback time to the Sparkler is 9.1 Gyr, and the age of the universe at that epoch is 4.6 Gyr. Distinguishing between $z = 3$ and $z = 9$ formation epochs for the globular cluster system corresponds to distinguishing between 2.4 Gyr and 4.1 Gyr old populations, which is relatively straightforward for population synthesis models in the JWST bands. In the case of the Sparkler, the striking conclusion is that at least foir of its globular clusters have likely formed at $z > 9$.

Our identification of the sparkles in Figure 1 with evolved globular clusters relies on an assumption of very strong magnification of the Sparkler. Strong magnification occurs only in narrow regions near lensing caustics, so there are strong magnification gradients in the source plane. This makes it difficult to invert lens models to compute accurate luminosity functions for the putative globular cluster population. Based on Figure 1, we assume the overall magnification of the system is large (at least a factor of 15), but handling the strong magnification gradients across the local environment of the Sparkler is beyond the scope of this paper. Assuming magnifications of 10–100, the stellar masses of these point sources fall in the range $\sim 10^6 – 10^7 \, M_\odot$, which is plausible for metal-poor globular clusters seen at ages of around 4 Gyr, although most lie at the high end of the local globular cluster mass range. Since a critical curve may be running through the system, we emphasize again that the magnification (and hence the masses) of the clusters is very uncertain.

If lens models can be determined with the accuracy needed to compute the source plane luminosity functions and mass distributions, then the Sparkler may place interesting constraints on globular cluster dissolution. Physical processes slowly dissolve globular clusters, and luminosity evolution is significant, so distant globular clusters are expected to be both more massive and more luminous than their local counterparts (Webb & Leigh 2015; Goudfrooij 2018). The most relevant physical processes are stellar evolution coupled with relaxation and tidal effects, and in some models significant mass loss is expected. For example, with a standard Kroupa initial mass function (IMF) (Kroupa 2001) about 30% of the mass of a star cluster is expected to be lost due to stellar evolution alone in the first few Gyr (Baumgardt & Makino 2003), and this fraction is much higher for top-heavy IMFs. Dynamical processes would compound this loss, though dynamical processes are likely to be most significant for lower-mass clusters (Baumgardt 2006). In any case, unless globular cluster dissolution processes are operating far more quickly than expected, very high magnifications are certainly needed to explain the point sources surrounding the Sparkler as globular clusters.

6. Conclusions

In situ investigations of evolved globular cluster systems at $z \sim 1.5$ present us with a golden opportunity to probe the initial formation epoch of globular clusters with a precision unobtainable from studying local systems. Magnified red point sources seen at this epoch are old enough to be unambiguously identified as globular clusters, but young enough that their ages can be determined quite reliably. We applied this idea to JWST and HST observations of a $z = 1.378$ galaxy (which we refer to as the Sparkler), which is strongly lensed by the $z = 0.39$ galaxy cluster SMACS0723. At least 5 of the 12 compact sources in and around the Sparkler are unresolved and red, and the most likely interpretation of these is that they are evolved globular clusters seen at $z = 1.378$. By modeling the colors and spectra of these compact sources with the DENSE BASIS method, four (33%) are found to be consistent with a SSP forming at $z > 9$, i.e., in the first 0.5 Gyr of cosmic history and more than 13 Gyr before the present epoch. If these ages are confirmed, at least some globular clusters appear to have formed contemporaneously with the large-scale reionization of the intergalactic medium, hinting at a deep connection between globular cluster formation and the initial phases of galaxy assembly. Data and code to reproduce our results will be made available at http://canucs-jwst.com/sparkler.html.

ORCID iDs

Lamiya Mowla ● https://orcid.org/0000-0002-8530-9765
Kartheik G. Iyer ● https://orcid.org/0000-0001-9298-3523
Guillaume Desprez ● https://orcid.org/0000-0001-8325-1742
Vicente Estrada-Carpenter ● https://orcid.org/0000-0001-8489-2349
Nicholas S. Martis ● https://orcid.org/0000-0003-3243-9969
Ghassan T. Sarrouh ● https://orcid.org/0000-0001-8830-2166
Victoria Strait ● https://orcid.org/0000-0002-6338-7295
Yoshihisa Asada ● https://orcid.org/0000-0003-3983-5438
Gabriel Brammer ● https://orcid.org/0000-0003-2680-005X
Marcin Sawicki ● https://orcid.org/0000-0002-7712-7857
Chris J. Willott ● https://orcid.org/0000-0002-4201-7367
Marusa Bradac ● https://orcid.org/0000-0001-5984-0395
René Doyon ● https://orcid.org/0000-0001-5485-4675
Adam Muzzin ● https://orcid.org/0000-0002-9330-9108
Camilla Pacifici ● https://orcid.org/0000-0003-4196-0617
Swara Ravindranath ● https://orcid.org/0000-0002-5269-6527
Johannes Zabl ● https://orcid.org/0000-0002-9842-6354

References

Astropy Collaboration, Price-Whelan, A. M., Sipőcz, B. M., et al. 2018, AJ, 156, 123
Astropy Collaboration, Robitaille, T. P., Tollerud, E. J., et al. 2013, A&A, 558, A33
Barbary, K. 2016, JOSS, 1, 58
Baumgardt, H. 2006, arXiv:0605125
Baumgardt, H., & Makino, J. 2003, MNRAS, 340, 227
Bennet, P., Alfaro-Cuello, M., del Pino, A., et al. 2022, ApJ, 935, 149
Bertin, E., & Arnouts, S. 1996, A&AS, 117, 393
Boylan-Kolchin, M. 2017, MNRAS, 472, 3120
Boylan-Kolchin, M. 2018, MNRAS, 479, 332
Bradley, L., Sipőcz, B., Robitaille, T., et al. 2021, astropy/photutils: 1.1.0, 1.1.0, Zenodo, Zenodo, doi:10.5281/zenodo.4624996
Brammer, G., & Matharu, J. 2021, gbrammer/grizli: Release 2021, 1.3.2, Zenodo, Zenodo, doi:10.5281/zenodo.5012699
Brammer, G. B., van Dokkum, P. G., & Coppi, P. 2008, ApJ, 686, 1503
Brodie, J. P., & Strader, J. 2006, ARA&A, 44, 193
Caminha, G. B., Suyu, S. H., Mercurio, A., et al. 2022, arXiv:2207.07567
Carballo-Bello, J. A., Gieles, M., Sollima, A., et al. 2012, MNRAS, 419, 14
Carlberg, R. G. 2002, ApJ, 573, 60
Caswell, T., Droettboom, M., Hunter, J., et al. 2019, matplotlib/matplotlib v3.1.0, Zenodo, doi:10.5281/zenodo.2893252
Coe, D., Salmon, B., Bradač, M., et al. 2019, ApJ, 884, 85
Conroy, C., Gunn, J. E., & White, M. 2009, ApJ, 699, 486
Conroy, C., White, M., & Gunn, J. E. 2010, ApJ, 708, 58
de Grijs, R., O'Connell, R. W., & Gallagher, J. S. I. 2001, AJ, 121, 768
Doyon, R., Hutchings, J. B., Beaulieu, M., et al. 2012, Proc. SPIE, 8442, 84422R
Erkal, D., Belokurov, V., Laporte, C. F. P., et al. 2019, MNRAS, 487, 2685
Ferland, G. J., Porter, R. L., van Hoof, P. A. M., et al. 2013, RMxAA, 49, 137
Forbes, D. A., Bastian, N., Gieles, M., et al. 2018, RSPSA, 474, 20170616
Foreman-Mackey, D. 2016, JOSS, 1, 24
Förster Schreiber, N. M., Genzel, R., Lehnert, M. D., et al. 2006, ApJ, 645, 1062
Freeman, K. C., & Norris, J. 1981, ARA&A, 19, 319
Genzel, R., Tacconi, L. J., Eisenhauer, F., et al. 2006, Natur, 442, 786
Golubchik, M., Furtak, L. J., Meena, A. K., & Zitrin, A. 2022, arXiv:2207.05007
Goudfrooij, P. 2018, ApJ, 857, 16
Harris, W. E., & Racine, R. 1979, ARA&A, 17, 241
Herrmann, K. A., Hunter, D. A., & Elmegreen, B. G. 2016, AJ, 151, 145
Iyer, K., & Gawiser, E. 2017, ApJ, 838, 127
Iyer, K., Gawiser, E., Davé, R., et al. 2018, ApJ, 866, 120
Iyer, K. G., Gawiser, E., Faber, S. M., et al. 2019, ApJ, 879, 116
Iyer, K. G., Gawiser, E., Faber, S. M., et al. 2021, dense_basis: Dense Basis SED fitting, Astrophysics Source Code Library, record ascl:2104.015
Johnson, B., Foreman-Mackey, D., Sick, J., et al. 2021, dfm/python-fsps: python-fsps v0.4.1rc1, Zenodo, doi:10.5281/zenodo.4737461
Johnson, C. I., Caldwell, N., Rich, R. M., et al. 2017, ApJ, 836, 168
Kroupa, P. 2001, MNRAS, 322, 231
Laporte, N., Zitrin, A., Dole, H., et al. 2022, arXiv:2208.04930
Leja, J., Carnall, A. C., Johnson, B. D., Conroy, C., & Speagle, J. S. 2019, ApJ, 876, 3
Livermore, R. C., Jones, T., Richard, J., et al. 2012, MNRAS, 427, 688
Livermore, R. C., Jones, T. A., Richard, J., et al. 2015, MNRAS, 450, 1812
Lower, S., Narayanan, D., Leja, J., et al. 2020, ApJ, 904, 33
Mahler, G., Jauzac, M., Richard, J., et al. 2022, arXiv:2207.07101
Ocvirk, P., Pichon, C., Lançon, A., & Thiébaut, E. 2006, MNRAS, 365, 46
Olsen, C., Gawiser, E., Iyer, K., et al. 2021, ApJ, 913, 45
Peebles, P. J. E., & Dicke, R. H. 1968, ApJ, 154, 891
Peng, C. Y., Ho, L. C., Impey, C. D., & Rix, H.-W. 2010, AJ, 139, 2097
Pontoppidan, K., Blome, C., Braun, H., et al. 2022, ApJL, 936, L14
Price, D. C., van der Velden, E., Celles, S., et al. 2018, JOSS, 3, 1115
Renzini, A. 2017, MNRAS, 469, L63
Rieke, M. J., Kelly, D., & Horner, S. 2005, Proc. SPIE, 5904, 1
Sameie, O., Boylan-Kolchin, M., Hopkins, P. F., et al. 2022, arXiv:2204.00638
Schweizer, F., & Seitzer, P. 1998, AJ, 116, 2206
Trujillo-Gomez, S., Kruijssen, J. M. D., Reina-Campos, M., et al. 2021, MNRAS, 503, 31
Vanzella, E., Calura, F., Meneghetti, M., et al. 2017, MNRAS, 467, 4304
Vanzella, E., Castellano, M., Bergamini, P., et al. 2022, arXiv:2208.00520
Virtanen, P., Gommers, R., Oliphant, T. E., et al. 2020, NatMe, 17, 261
Walt, S. v. d., Colbert, S. C., & Varoquaux, G. 2011, CSE, 13, 22
Weaver, J. R., Kauffmann, O. B., Ilbert, O., et al. 2022, ApJS, 258, 11
Webb, J. J., & Leigh, N. W. C. 2015, MNRAS, 453, 3278
Welch, B., Coe, D., Zitrin, A., et al. 2022a, arXiv:2207.03532
Welch, B., Coe, D., Diego, J. M., et al. 2022b, Natur, 603, 815
Willott, C. J., Doyon, R., Albert, L., et al. 2022, PASP, 134, 025002
Wuyts, E., Rigby, J. R., Gladders, M. D., & Sharon, K. 2014, ApJ, 781, 61